

# Quasiperiodic nondipole ionization dynamics in the x-ray stabilization regime

Aleksandr V. Boitsov,\* Karen Z. Hatsagortsyan,† and Christoph H. Keitel  
*Max-Planck-Institut für Kernphysik, Saupfercheckweg 1, 69117 Heidelberg, Germany*  
(Dated: February 9, 2026)

Recent advances in strong x-ray laser techniques enable the study of nonlinear multiphoton ionization in extreme high-frequency fields. Although the stabilization regime in such fields is theoretically established, its modified properties in the nondipole regime for long laser pulses remains unknown. Here, we numerically investigate the strong-field ionization of an atom in a long XUV laser pulse in the nondipole regime. Our study of the time-dependent quantum dynamics reveals a quasiperiodic modulation of the ionization yield as a function of pulse duration. We demonstrate that the Coulomb-field-induced slow oscillation of the ionized electron wave packet during the interaction is responsible for the observed modulation of the ionization yield. Furthermore, we scrutinize the unusual photon momentum sharing between the photoelectron and the ion in this extreme regime. These effects are observable in upcoming x-ray free-electron laser facilities.

## I. INTRODUCTION

Extremely nonlinear phenomena of the strong field ionization are well investigated with infrared and mid-infrared laser fields resulting in the emergence of attoscience [1–7]. However, recent advancement of strong laser techniques in the XUV and x-ray domain, in particular, the development of XFEL facilities in DESY [8], SLAC [9], and other places over the world [10, 11], has raised hopes to achieve the nonlinear multiphoton interaction regime of ionization with x-rays [12].

In high-frequency laser fields when the laser frequency  $\omega$  exceeds the atomic ionization energy  $I_p$ , the strong field ionization can enter into the so-called stabilization regime [13–15]. In this case, as the electron oscillation amplitude in the laser field  $\alpha_0 = E_0/\omega^2$  overtakes the atomic size  $a_s$ , the average effect of the atomic potential on the electron can be described by a dichotomic Kramers-Henneberger potential [16, 17]. Here,  $E_0$  is the laser field amplitude, and atomic units are used throughout. In this regime, the ionization probability saturates, remaining stable despite the increasing laser intensity. The photoelectron spectrum in the stabilization regime is characterized by a large near-zero energy peak [18] which is followed by the weak above-threshold ionization (ATI) peaks [19].

The early works already showed that the nondipole effects tend to significantly modify and even suppress the stabilization [20–24]. The nondipole effects in a strong laser field enter into play when the classical strong field parameter is large with  $a_0 := E_0/(c\omega) \gtrsim 1$  [25], where  $c$  is the speed of light. This condition is easier to achieve at low frequencies, for instance,  $a_0 \sim 1$  is achieved in infrared laser fields with a wavelength  $\lambda = 1000$  nm at a laser intensity  $I \sim 10^{18}$  W/cm<sup>2</sup>, while for x-rays  $\lambda = 10$  nm, this would require  $I \sim 10^{22}$  W/cm<sup>2</sup>, which could be envisaged with the development of x-ray focusing technique [26].

Ionization in the nondipole regime shows distinctive features already at  $a_0 \gtrsim 0.1$  due to the relativistic drift induced by the  $v \times B$  Lorentz force. It breaks the symmetry of the system with

respect to the laser field direction [23], and leaves signatures in the photoelectron momentum distribution (PMD). The numerical calculations of the time-dependent Schrödinger equation (TDSE) in a perturbatively weak x-ray field [27] reveal that the PMD is shifted along the laser propagation direction, similar to ATI in infrared fields [28, 29], when the forward ionization is preferred with respect to the backward one. In stronger non-perturbative x-ray fields an interesting interplay between the nondipole and Coulomb fields has been observed in Ref. [30], demonstrating counterintuitive features in the photoelectron angular distribution (PAD). In particular, two lobes in PAD, which in the dipole case are perpendicular to the laser wave propagation direction, are bent towards the direction opposite to the laser propagation, and additionally a new third lobe appears along that direction. This counterintuitive behavior has been explained by the effect of the Coulomb forces of the atomic core. While the laser magnetic field induces the continuum wave packet drift in the laser propagation direction, the created asymmetry produces a net Coulomb force acting on the wave packet in the opposite direction, which yields the generation of the anomalous lobe in the PAD. Later results of Refs. [19, 31] confirmed this effect and noted that the anomalous lobe increases with increasing the laser pulse duration within limited range. It is worth to underline that the above-mentioned counterintuitive behavior is general for strong field interaction and has been observed also at infrared laser fields [32], when a counterintuitive shift of the peak of the photoelectron momentum distribution (PMD) is observed due to nondipole asymmetry.

The role of the relativistic effects has been discussed in Refs. [19, 33] solving the time-dependent Dirac equation (TDDE). In particular, a spin-flip effect is analyzed in [33] showing that it is extremely small by a factor of  $10^{-6}$  at the x-ray field of  $a_0 \approx 0.05 - 0.15$ . The findings of [30, 31] have been confirmed in the fully relativistic framework. Despite a great attention to the nondipole ionization in a strong x-ray field, the dependence of the ionization probability on the pulse duration largely remained unexplored.

Strong-field ionization of an atom takes place due to absorption of laser photons. In the nondipole regime the photon momentum cannot be neglected. Then a question arises how the linear momentum of absorbed photons is partitioned between the constituents of the atom, between the ionized electron and

\* boitsov@mpi-hd.mpg.de

† k.hatsagortsyan@mpi-hd.mpg.de

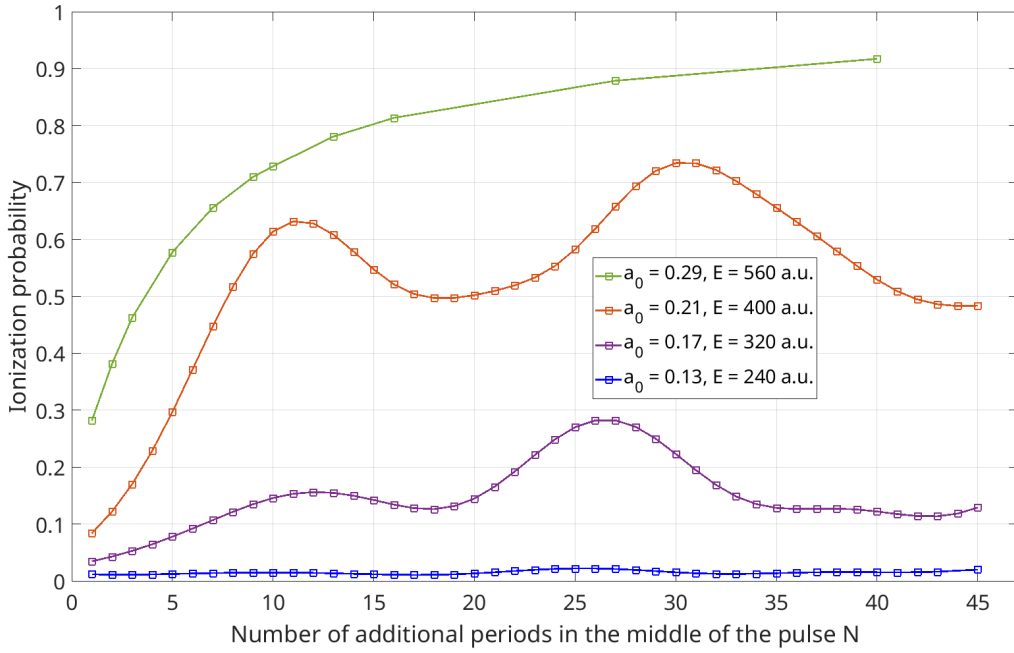


FIG. 1. **The dependence of the ionization probability of hydrogen-like helium on the laser pulse duration.** Each line represents a different  $a_0$  parameter indicated in the inset,  $a_0 = 0.13 - 0.29$  corresponding to the intensity range of  $I = 2 \times 10^{21} - 1.1 \times 10^{22} \text{ W/cm}^2$ . The duration of the pulse is  $T = NT_0 + 4\tau$ . The laser frequency is  $\omega = 14 \text{ a.u.}$

the emerged ion. While this question is well investigated in the case of the strong-field ionization with infrared laser fields, or in the case of the photoeffect [34–43] – single photon ionization with an XUV photon, in the case of the stabilization regime in strong XUV fields, when the large momentum exchange between the photoelectron and ion via Coulomb interaction non-trivially modifies the momentum sharing, has not been addressed.

In this paper, we investigate the role of the laser pulse duration in the strong x-ray field ionization of an hydrogen-like ion in the stabilization regime. By changing the driving pulse duration in a wide range up to 45 optical cycles, we reveal a slow periodic variation of the ionization yield with respect to the pulse duration. It turns out that the yield oscillation exists both in the dipole and nondipole regimes, however, with different oscillation features and with different underlying mechanisms. While in the dipole regime the oscillation of the ionization yield is explained by the known dynamic interference phenomenon [44–49], combined with the internal dynamics of the Kramers-Henneberger (KH) atom, in the nondipole regime this explanation fails, because of the suppression of the dynamic interference due to the relativistic drift. The distinctive mechanism, which brings about the ionization yield oscillation in the nondipole regime, is the slow orbiting of the continuum electron wave packet during the interaction mostly in the propagation direction, which is induced by the Coulomb field of the atomic core combined with the nondipole drift. We investigate also the photon momentum partition between the photoelectron and ion in this extreme stabilization regime. Our investigation is based on the numerical solution of the Foldy-Wouthuysen

transformed TDDE in the 2D case in the quasiclassical representation of Silenko [50–52]. The numerical calculations are facilitated by the application of the coordinate scaling method [53].

The article is structured as follows: in Sec. II the results of our numerical simulations are presented. The explanation of the yield oscillation in the dipole regime is discussed in Sec. III, and in the nondipole regime in Sec. IV. In Sec. V the question of the photoelectron-ion momentum sharing is addressed. The brief presentation of the calculation method is given in Appendix.

## II. IONIZATION YIELD VS INTERACTION TIME

We consider the hydrogen-like atom interaction with a strong laser field in the nondipole stabilization regime, when  $\omega > I_p$ ,  $a_0 \gtrsim a_s = 1/Z$ , with the charge  $Z$  of the atomic core. The following typical parameters for the stabilization regime are used:  $\omega = 14 \text{ a.u.}$  (381 eV),  $E_0 = 240 - 560 \text{ a.u.}$  ( $I = 2 \times 10^{21} - 1.1 \times 10^{22} \text{ W/cm}^2$ ). In this case we have the strong field parameter  $a_0 = 0.13 - 0.29$ , and the electron oscillation amplitude  $a_0 \approx 1.22 - 2.85$ . We calculated the ionization yield in laser pulses of different duration via evaluating the bound state populations after the interaction. Hydrogen-like helium ( $Z = 2$ ) is chosen as a model to have a pronounced Coulomb effect, which we will see is important for the considered effect.

The ionization yield dependence on the laser pulse duration at different laser fields is shown in Fig. 1. The laser pulse is

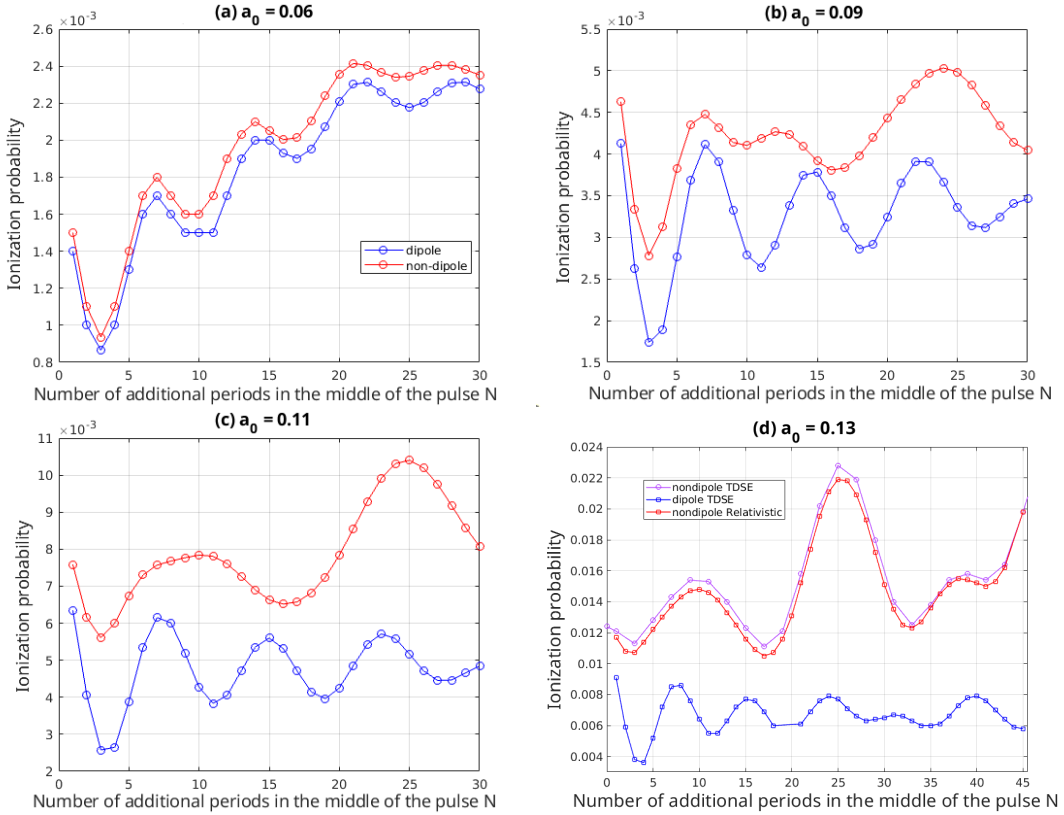


FIG. 2. Comparison of the dipole and nondipole calculations for the ionization probability vs the laser pulse duration. (a)  $a_0 = 0.06$ ,  $E = 120$  a.u., (b)  $a_0 = 0.09$ ,  $E = 180$  a.u., (c)  $a_0 = 0.11$ ,  $E = 210$  a.u., (d)  $a_0 = 0.13$ ,  $E = 240$  a.u.; (blue line) – dipole approximation, (red line) – nondipole calculations. Duration of the pulse is  $T = NT_0 + 4\tau$ ,  $\omega = 14$  a.u.

of a trapezoidal form, see Appendix, with the duration  $T = NT_0 + 4\tau$ , where  $T_0 = 2\pi/\omega$  is the laser field period,  $\tau = 2.5T_0$  is the switching-on and -off parameter of the laser pulse, and  $N$  is the number of cycles in the flat region of the pulse. One can see that the ionization yield oscillates with the number of cycles. The period of oscillations increases with larger  $a_0$ , indicating that it is a nondipole effect, possibly connected with the nondipole drift in the laser propagation direction  $z$ . The modulation depth of the oscillations increases up to  $a_0 = 0.2$ , with further damping at larger  $a_0$ . The latter indicates that there is another effect involved in the process which counteracts and competes with the nondipole drift.

As Fig. 1 points out the nondipole character of the oscillating yield effect, one could expect that it vanishes in the dipole case. In Fig. 2(d) we compare the relativistic calculation with the nondipole and the dipole ones. Surprisingly, the yield oscillation exists also in the dipole case, however, with a significant difference in the period, amplitude and shape of the oscillations compared with the nondipole case.

One can note [Figs. 1, 2] that the nondipole character of the field leads to the increase of the ionization yield, which naturally is explained by the effect of the nondipole drift. The latter results in the shift of the wave packet average coordinate from the atomic core at the end of the pulse, which hinders the recombination of the wave packet and enhances the ionization, because in the stabilization regime it emerges mostly

during switching-on and -off of the laser field [15]. Fully relativistic treatment yields a slightly suppressing of the ionization, because the relativistic mass correction slightly hinder the drift.

### III. DIPOLE REGIME

Let us firstly examine the origin of the ionization yield oscillation in the dipole case [Fig. 2(d)]. In the dipole calculation, the ionization probability oscillates near an average value  $w_i \approx 0.7\%$ . The oscillations seem to have a constant period  $\mathcal{T} \approx 8T_0 \approx 3.59$  a.u., independent of the total duration of the pulse. For more information, we analyze the photoelectron energy distribution (PED) in the dipole case in Fig. 3. The chosen pulse durations correspond to the local maxima or minima of the ionization probability from Fig. 2(d) (blue line). We show PED near the zero-energy peak (ZEP) ( $\varepsilon \ll \omega$ ), which contains most of the ionization probability, see Table I.

Firstly, we note in Fig. 3 that the spectral density vanishes at the continuum threshold,  $\varepsilon = 0$ , which is in accordance with the PED scaling at the threshold at high laser frequencies  $\omega > I_p$  [18]. In our numerical calculation this property is due to the fact, that the positive and negative regions of the wave function cancel each other (with up to 3 digits of accuracy), while integrating over the space. In Fig. 3 we see modulation of the PED with the period  $\delta\varepsilon = 2\pi/\mathcal{T}$ , related to the pulse duration

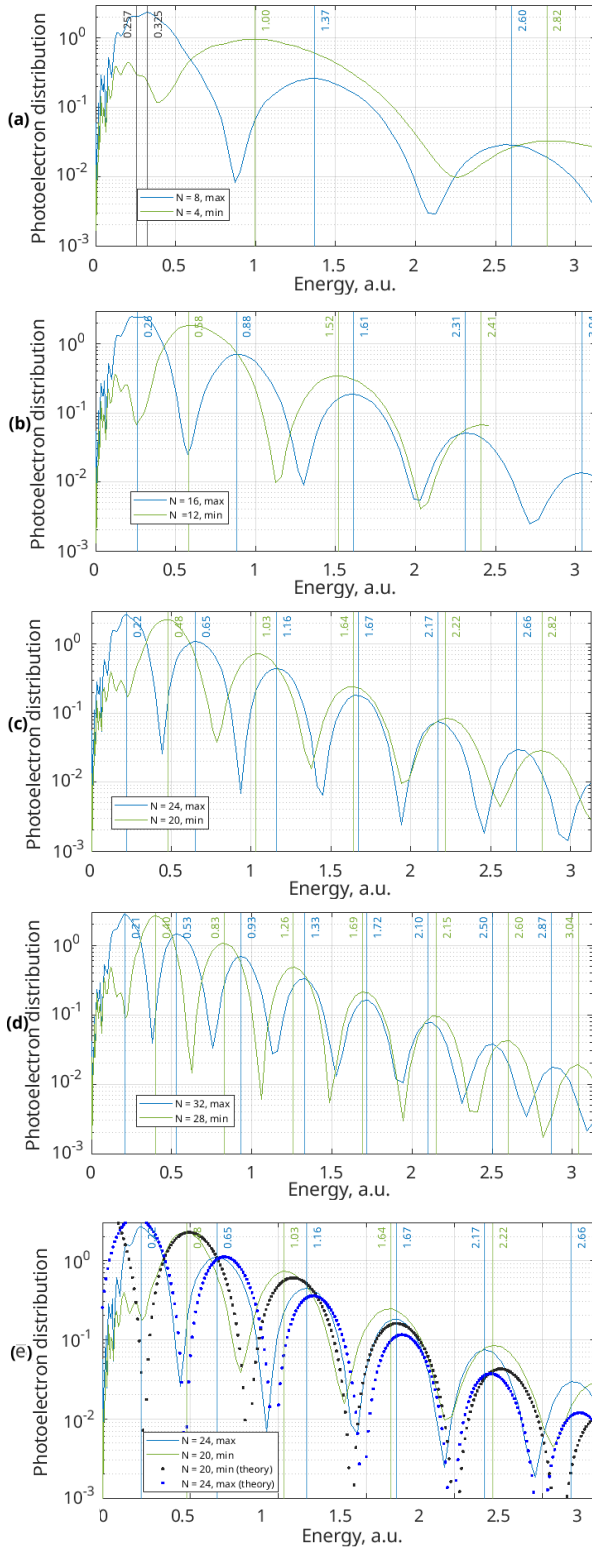


FIG. 3. **Photoelectron momentum distributions (PED) in the dipole case.** PED near ZEP in the dipole calculations at different pulse durations,  $a_0 = 0.13$ ,  $\omega = 14$  a.u.: (a)-(d) The number of cycles  $N$  is indicated in the insets and corresponds to the maxima and minima of the ionization probabilities of Fig. 2; (e) Comparison of the dynamic model Eq. (2) (dotted line) with PEDs.

$\frac{N}{a_0}$	1	5	12	20
0.06	0.27	0.42	0.55	0.61
0.09	0.07	0.10	0.13	0.16
0.11	0.05 (0.04)	0.09 (0.05)	0.13 (0.06)	0.14 (0.08)
0.13	0.03 (0.002)	0.07 (0.003)	0.09 (0.003)	0.10 (0.005)

TABLE I. **The ratio of the probability in the above-threshold ionization (ATI) peaks with respect to the total ionization probability.** The values are for the dipole case, and in brackets for the nondipole case (where applicable). For the small  $a_0$  value, an ATI channel dominates ionization, which explains a steady growth in the Fig. 2(a).

$T = NT_0 + 2\tau$ , which is in accordance with the dynamic interference picture [44–49] (we assume the ionization happens in a half-way of switching on the laser pulse). The total width of the near-zero-energy distribution is related to the switching-on time  $\tau$ :  $\Delta\epsilon \sim 2\pi/\tau = \omega/2.5 \approx 5.6$  a.u. Thus, the main ionization yield comes from the near-zero-energy distribution of the spectrum, which has a constant bandwidth for the given switching on time. The modulation of the near-zero-energy distribution has an important feature: the first modulation peak in the case of the maximum ionization yield is always closer to the peak of the near-zero-energy distribution and larger by magnitude than that in the minimum case and this is the reason for the ionization yield oscillation with respect to the pulse duration.

To explain the feature mentioned above, we look more closely at the dynamic interference picture, when the ionization unfolds mainly during the pulse turn-on and turn-off regions:

$$f(t) = f_1(t) + f_1(t - T)e^{-i\Omega T}, \quad (1)$$

where  $f(t)$  is the time-dependent ionization amplitude,  $T$  is the time between the start and the end of the pulse, and for concreteness, we use  $f_1(t) = 1/[1 + (t/\tau)^2]$ . The spectra in Fig. 3 are recovered introducing the phase  $\phi = \Omega t$  for the ionization contribution at switching-off the laser pulse, which effectively takes into account the periodic character of the ionization process with frequency  $\Omega = 2\pi/\mathcal{T} = 1.75$  a.u.,

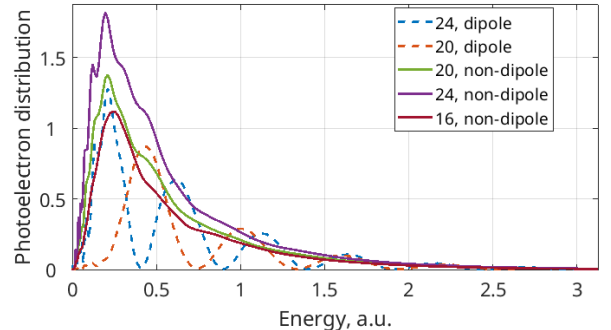


FIG. 4. **Photoelectron momentum distributions (PED) in the nondipole regime.** PED for different pulse durations indicated in the inset:  $a_0 = 0.11$ . The dipole calculations are shown by the dashed lines, the nondipole by the solid ones.

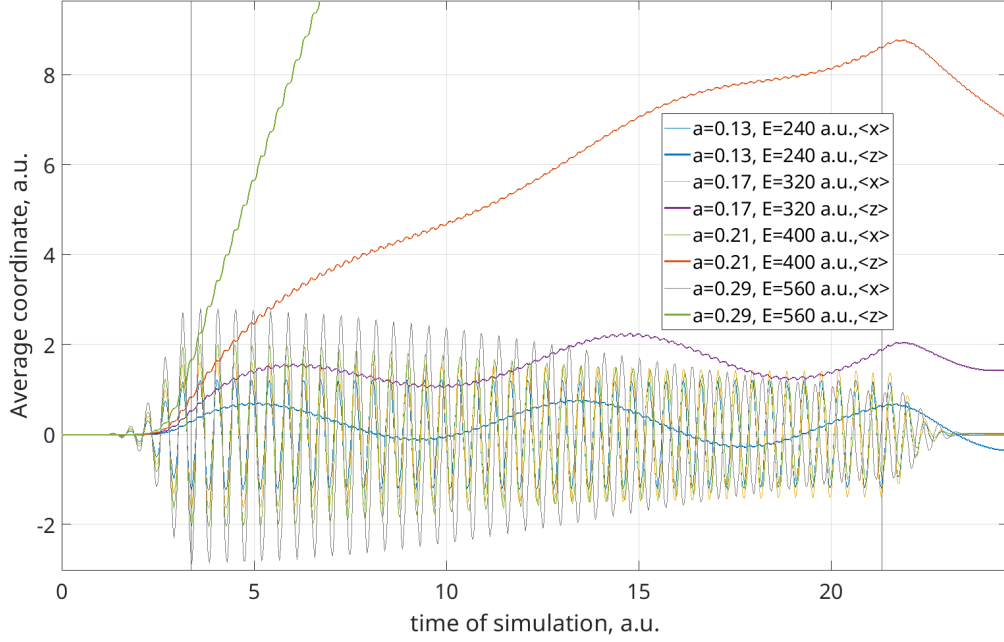


FIG. 5. **The expectation value for the electron coordinates during the interaction.** The coordinate in the laser polarization direction is  $\langle x(t) \rangle$ , and along the propagation direction  $\langle z(t) \rangle$ . Different lines represent different  $a_0$  values indicated in the inset. The frequency is  $\omega = 14$  a.u.

according to Fig. 2. Then, the PED is given by

$$S(\varepsilon) = S_1(\varepsilon) + S_1(\varepsilon)e^{i(\varepsilon-\Omega)T}, \quad (2)$$

with  $S(\varepsilon) = \int f(t)e^{i\varepsilon t} dt$ , and  $S_1(\varepsilon) = e^{-\varepsilon/\tau}$ . The simple heuristic model of Eq. (2) recovers the numerically obtained spectral shape, with peak positions  $\varepsilon_n = \Omega + (2\pi/T)n, n \in \mathbb{Z}$ , see Fig. 3(e), and ensures that the first peak in the case of the maximum ionization yield is closer to zero than in the case of the minimum, as observed in the PEDs. Note that  $\Omega = 1.75$  and  $n = 0$  corresponds to a high-order peak in PED (it is fixed at any pulse duration), while the first peak in the PED in the case of minimum yield are obtained at  $n = -T/\mathcal{T}$ , with  $\varepsilon_n \approx 0$  (this threshold peak is suppressed).

The origin of the periodic term  $e^{-i\Omega T}$  in the ionization yield of Eq. (1) probably stems from the bound state periodic dynamics in the KH potential during the interaction [54], with the parameter  $\mathcal{T}$  related to the energy difference of the populated KH states.

#### IV. NONDIPOLE REGIME

##### A. General features

The transition from the dipole to the nondipole regime at increasing  $a_0$  is illustrated in Fig. 2(a-d) for the ionization yield. In the nondipole regime, there are also the ionization yield oscillations with respect to the interaction time, which have larger amplitude and longer periodicity. Also, the nondipole effect doubles the ionization probability,  $w_i \approx 1.4\%$ , for the

case  $a_0 = 0.13$ . For the lowest presented  $a_0 = 0.06$ , we see that the ionization probabilities for the dipole and nondipole case follow the same pattern with the pulse duration. For the intermediate  $a_0 = 0.09$ , the plots are different by a constant for the short laser pulses  $N < 10$ , but the deviation becomes nontrivial for  $N > 18$ . At  $a_0 = 0.109$ , the dipole and nondipole behaviors follow different pattern.

Increasing the parameter  $a_0$  further up to 0.29 [Fig. 1], we observe a dramatic change of the ionization probability comparing to the dipole case. While at  $a_0 = 0.13$ , the yield behavior is still similar to its dipole counterpart, at  $a_0 = 0.17$  it starts to exhibit both oscillations and a smooth increase, which is more pronounced at  $a_0 = 0.21$ . At  $a_0 = 0.29$ , we see a change of the pattern again. There are no more large oscillations and the ionization gradually increases with respect to the pulse duration up to the saturation.

The PED in the nondipole case, see Fig. 4, in contrast to the dipole case, is dominated by a single low energy broad distribution, coinciding with the bandwidth of the dipole PED  $\Delta\varepsilon \sim 2\pi/\tau$ , without significant modulation due to the dynamic interference. Thus, the dynamic interference cannot be the main cause for the yield oscillation in the nondipole regime.

To analyze the nondipole features of the dynamics, we inspect the expectation values of the coordinates for the electron wave packet in the continuum during the interaction. The typical trajectories via the expectation value of the coordinates in the laser polarization direction  $\langle x(t) \rangle$ , and the propagation direction  $\langle z(t) \rangle$  for  $a_0 = 0.13 - 0.29$  are shown in Fig. 5.

The main difference of  $\langle x(t) \rangle$  from the dipole regime becomes visible only for  $a_0 > 0.17$ , namely the amplitude of

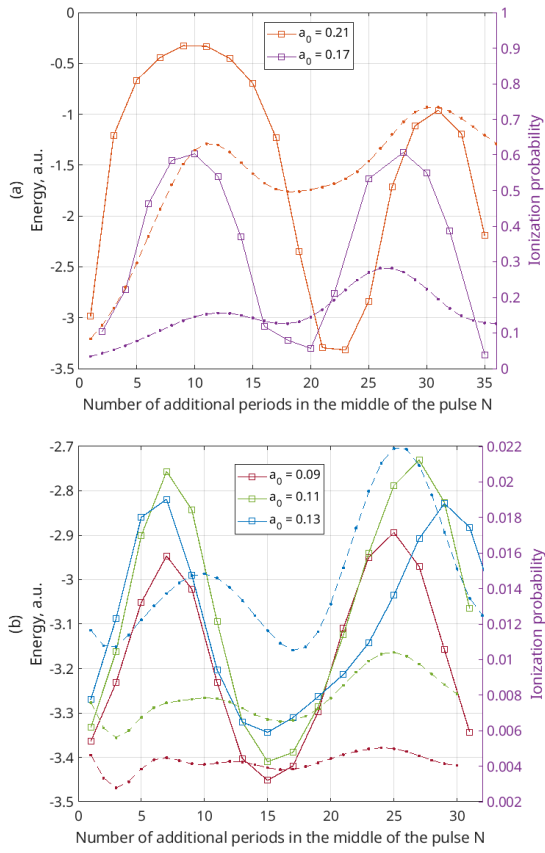


**FIG. 6. The electron energy after the interaction as a characteristic parameter of the ionization yield.** The expectation value of the electron energy  $\langle \epsilon \rangle$  of the electron wave packet  $t = 10$  a.u. after the interaction vs. the laser pulse duration (solid lines): (a)  $a_0 = 0.17$  (violet),  $a_0 = 0.21$  (red), (b)  $a_0 = 0.09$  (red),  $a_0 = 0.11$  (green),  $a_0 = 0.13$  (blue). The corresponding ionization yields are shown in the panels as dashed lines.

the oscillations starts gradually decreasing. This is a purely quantum nondipole effect. As the electron wave packet is not localized in space, its different parts are exposed to the different values of the nondipole field, tending to decrease oscillations of an electron in space with time.

For the expectation value  $\langle z(t) \rangle$ , the situation is less trivial. In case of the absence of the atomic potential, the electron would experience a magnetically induced drift in the laser propagation  $z$  direction with an average speed  $v_z(t) = e^2 A_x^2(t)/(4c)$  [55]. However, the atomic potential counteracts the laser induced drift, which results in the generation of the electron slow oscillations along the  $z$  coordinate, with a frequency much smaller than the laser frequency. At larger  $a_0$ , the drift compensation fails and the drift component in  $\langle z(t) \rangle$  starts to dominate, see the case  $a_0 = 0.29$  in Fig. 5.

The periodic oscillation of the expectation value of  $\langle z(t) \rangle$  for the electron wave packet during the interaction results in the oscillation of  $\langle z \rangle$ , as well as the average energy  $\langle \epsilon \rangle = \langle p_z^2 \rangle/2 + \langle V(z) \rangle$ , at the switching-off of the laser field. In the stabilization regime when the main ionization takes place at

the switching-on and -off of the laser pulse, the final coordinate and, hence, the energy oscillation yield a different probability of capturing the electron by the atomic field, and result in the oscillation of the ionization yield, see Fig. 6. The latter shows that the maximum  $\langle \epsilon \rangle$  is correlated with the maximum ionization yield, and it can serve as a characteristic parameter for the ionization yield.

## B. Nondipole regime: Coulomb momentum transfer

It is known that the Coulomb effects play an essential role for the strong field ionization in the stabilization regime [30]. The photoelectron momentum distribution (PMD) in this case shows an additional lobe into the direction opposite to the laser propagation direction, see Fig. 7 (the appearance of the interference structures in PMD are discussed in Ref. [49]). This counterintuitive behavior is the result of the interplay between the electromagnetic and Coulomb forces. Due to the nondipole drift the electron spends more time during the interaction at  $z > 0$  and experience the Coulomb momentum transfer (CMT) in the opposite direction. Moreover, the classical trajectories of ionized electrons which contribute to the anomalous nondipole lobe in PMD will be captured in the case of the dipole interaction. The larger the Coulomb momentum transfer during the interaction is, the larger will be the contribution into the PMD anomalous lobe. Therefore, we anticipate that the CMT during the interaction will provide an additional characteristic parameter for the ionization yield in the nondipole regime  $a_0 \gtrsim 0.1$ . We calculate CMT during the interaction

$$\langle \mathbf{p}^C(t) \rangle = - \int_{-\infty}^t dt \langle \nabla V(r) \rangle, \quad (3)$$

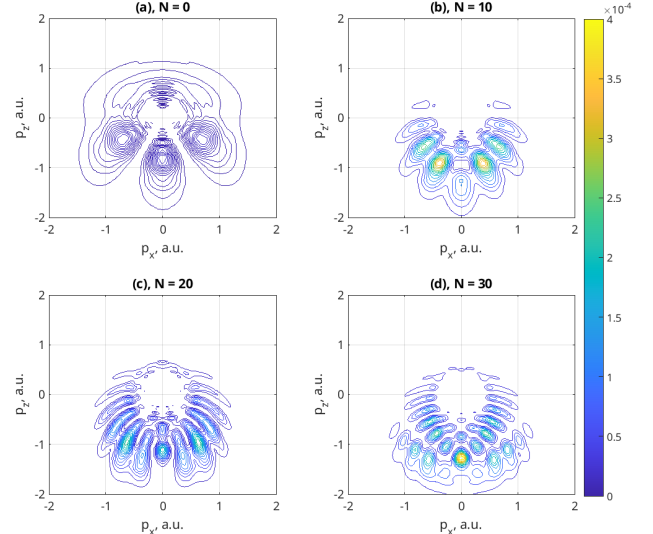


**FIG. 7. Photoelectron momentum distributions (PMD) for different durations of the pulse.** (a)  $N = 0$ , (b)  $N = 10$ , (c)  $N = 20$ , (d)  $N = 30$ . The parameters are:  $a_0 = 0.21$ ,  $\omega = 14$  a.u., corresponding to the red line in Fig. 1 and Fig. 5.

where the expectation value of the Coulomb force  $\langle -\nabla V(r) \rangle$  is calculated with the electron wave packet. The total values of CMT  $\langle p_z^C \rangle$  after the end of the interaction for  $a_0 = 0.17$  and  $a_0 = 0.21$  are presented in Fig. 8(a). For the both cases, the expectation value of the momenta of the final electron wave packet  $\langle p_z \rangle$  and the Coulomb induced momenta Eq. (3) nearly coincide. At  $a_0 = 0.21$  there is a good correlation to the ionization yield. At  $a_0 = 0.17$  the correlation is mostly qualitative. This is because the CMT of Eq. (3) is calculated via the total wave function of the electron, but the part of it recombines to the ground state after the interaction. Thus, we can take the total CMT  $\langle p_z^C \rangle$  as a characteristic parameter for the ionization in the nondipole regime when the ionization yield is significant and is mostly determined by the ZEP.

In the case of  $a_0 = 0.21$ , from one side the CMT shows well-defined oscillations with respect to the interaction time [Fig. 8(a)], but from another side  $\langle z(t) \rangle$  increases almost

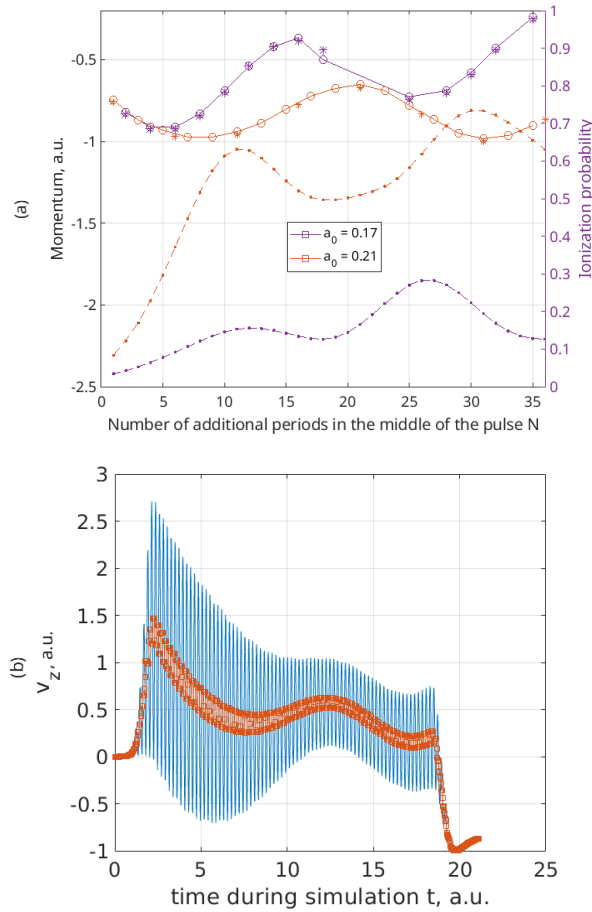


**FIG. 8. Correlation between the Coulomb momentum transfer (CMT) during the interaction and the ionization yield in the nondipole regime.** (a) CMT (stars),  $\langle p_z \rangle$  (solid lines) and the ionization yield (dashed lines) vs the pulse duration, (violet)  $a_0 = 0.17$ , (red)  $a_0 = 0.21$ , the corresponding ionization yields are shown as dashed lines; (b) Average velocity  $\langle v_z(t) \rangle$  of the electron wave packet vs the interaction time: Blue line is  $\langle v_z(t) \rangle$ , the red line is an averaged  $\langle v_z(t) \rangle$  over the fast oscillations,  $a_0 = 0.21$ ,  $\omega = 14$  a.u..

monotonously with the interaction time [Fig. 5], which would raise a question on the source of CMT. It is right that  $\langle z(t) \rangle$  (and the distance from the core) increases with the interaction time due to the nondipole drift, however, the dynamics includes additionally slow oscillation induced by the Coulomb force. Due to the latter the electron wave packet is slowed down at the turning points of the Coulomb induced orbiting, remains a long time at the same position, and acquires a large CMT. This is confirmed by Fig. 8(b) showing that the CMT is correlated with the slowing down of  $\langle v_z \rangle$ .

### C. Coulomb oscillations of the electron wave packet in continuum

We have seen, that the ionization yield oscillation in the nondipole regime depends on the laser pulse duration and is related to the periodic oscillatory dynamics of the electron wave packet in the laser propagation direction [Fig. 5]. The latter results in the oscillating energy and CMT at the end of the laser pulse, which finally has an impact on the ionization yield. Here, we examine more closely the slow quasiperiodic Coulomb oscillation dynamics, averaged over the fast laser driven oscillations along  $x$ , which arises as a result of the competition between the laser induced drift along  $z$  coordinate and the Coulomb force. To this end, we invoke Ehrenfest equation for the expectation values:

$$\frac{d\langle \mathbf{v}(t) \rangle}{dt} = -\langle E(\mathbf{r}, t) \rangle - \frac{1}{c} \langle \mathbf{v}(t) \times \mathbf{B}(\mathbf{r}, t) \rangle - \langle \nabla V(r) \rangle, \quad (4)$$

which reads in the components as

$$\begin{aligned} \frac{d^2\langle x(t) \rangle}{dt^2} &= -\left(1 - \frac{\langle v_z \rangle}{c}\right) E_0 \sin \omega t - \langle \partial_x V(x, z) \rangle \\ \frac{d^2\langle z(t) \rangle}{dt^2} &= -\frac{\langle v_x \rangle}{c} E_0 \sin \omega t - \langle \partial_z V(x, z) \rangle, \end{aligned} \quad (5)$$

where  $V(x, z) = Z / \sqrt{x^2 + z^2 + a_s^2}$ , with the nuclear charge  $Z = 2$ , and the atomic size (soft core parameter)  $a_s = \sqrt{3}/Z$  a.u. and we have taken into account the nondipolness of the interaction including the laser magnetic field.

In order to solve Eq. (5) as a classical equation, we employed an approximation for the expectation value of the Coulomb force  $-\langle \partial_x V(x, z) \rangle$ . We apply different approximations at  $a_0 \ll 1$  (see the cases  $a_0 \lesssim 0.13$  in Fig. 5), and at  $a_0 \sim 0.2$  (the cases  $a_0 = 0.17$  and  $a_0 = 0.21$  in Fig. 5). In the first case the typical size of the coordinate oscillation is less than the initial electron wave packet size as well as that throughout the interaction. Then, we introduce an effective atomic potential by means of smoothing the original soft-Coulomb atomic potential with an original ground state  $\psi_0(\mathbf{r})$  as

$$\langle V(\mathbf{r}) \rangle = \int_0^\infty V(\mathbf{r}') |\psi_0(\mathbf{r} - \mathbf{r}')|^2 d\mathbf{r}'. \quad (6)$$

We may estimate the condition for this regime as  $a_0 \sim a_s$ , which yields

$$a_0 \sim \frac{\sqrt{3}\omega}{cZ} \approx 0.1, \quad (7)$$

for our parameters  $Z = 2$  and  $\omega = 14$ . In the opposite case, the oscillation typical size along  $z$  axis is larger than the initial electron wave packet size [Fig. 5]. Then, the electron wave packet is relatively compact during the interaction and we use the approximation

$$-\langle \partial_x V(x, z) \rangle \approx -\partial_x V(\langle x \rangle, \langle z \rangle) \quad (8)$$

We calculate the numerical solution of Eq. (5) with either the effective potential of Eq. (6), or with Eq. (8). The corresponding calculated oscillation periods are shown in Fig. 9 as blue and magenta lines.

To obtain the scaling for the slow oscillation parameters, we apply an analytical analysis, seeking for an analytical approximate solution for the coordinate expectation values, representing it as slow and fast motions:

$$\langle x(t) \rangle = X(t) + \xi(t), \quad \langle z(t) \rangle = Z(t) + \zeta(t), \quad (9)$$

where fast motion  $\xi(t), \zeta(t)$  is characterized by the time scale of the laser period  $T_0$ . We insert the ansatz Eq. (9) into Eq. (5), and average over the fast oscillations. We assume that the laser field dominates the Coulomb one  $E_0 \gg E_a$ , with the atomic field  $E_a = Z/a_s^2$  then the fast oscillations are described only by the laser field

$$\xi(t) = \alpha_0 \sin \omega t, \quad (10)$$

$$\zeta(t) = \frac{ca_0^2}{4\omega} \sin 2\omega t. \quad (11)$$

The laser induced nondipole drift  $\mathcal{Z}_L = v_{zd}t$ , with  $v_{zd} = ca_0^2/(4 + a_0^2)$  [55], is included in the slow dynamics. Since  $\ddot{\mathcal{Z}}_L = 0$ , the electron slow motion as a result of competition of the laser induced drift and the Coulomb attraction is described as

$$\ddot{\mathcal{Z}} = -\partial_Z \bar{V}(\mathcal{Z}, \alpha_0) \quad (12)$$

where the laser induced drift is accounted for via the initial condition  $\bar{\mathcal{Z}}(0) = v_{zd}$ . Here, the overline indicates averaging over the fast oscillations.  $\bar{V}(\mathcal{Z}, \alpha_0)$  depends on the distance from the potential center  $r$ , which can be approximated as  $r^2 = (X + \xi)^2 + (\mathcal{Z} + \zeta)^2 + a_s^2 \approx \xi^2 + \mathcal{Z}^2 + a_s^2$ , taking into account that  $|X| \ll |\xi(t)|$ , and  $|\zeta(t)| \ll |\mathcal{Z}|$ , which is in accordance with the results of Fig. 5. The averaged Coulomb potential can be presented as

$$\begin{aligned} \bar{V}(\mathcal{Z}, \alpha_0) &\approx \frac{1}{T_0} \int_0^{T_0} dt' \frac{Z}{\sqrt{\xi(t')^2 + \mathcal{Z}^2 + a_s^2}}, \\ &= -\frac{4Z}{\sqrt{a_s^2 + \mathcal{Z}^2}} K\left(-\frac{a_0^2}{a_s^2 + \mathcal{Z}^2}\right) \end{aligned} \quad (13)$$

where  $K(\cdot)$  is the complete elliptic integral of the first kind.

In the limit  $a_0 \ll 1$ , the laser drift is not large  $|\mathcal{Z}_L| \ll |\mathcal{Z}| \ll \alpha_0$  and the KH force can be expanded with respect to the small parameter  $|\mathcal{Z}_L|/\alpha_0$ :  $-\partial_Z \bar{V}(\mathcal{Z}) \approx -[Z/(a_s^2 + a_0^2)^{3/2}]\mathcal{Z}$ , which results in the harmonic slow oscillations

$$\ddot{\mathcal{Z}} + \Omega^2 \mathcal{Z} = 0, \quad (14)$$

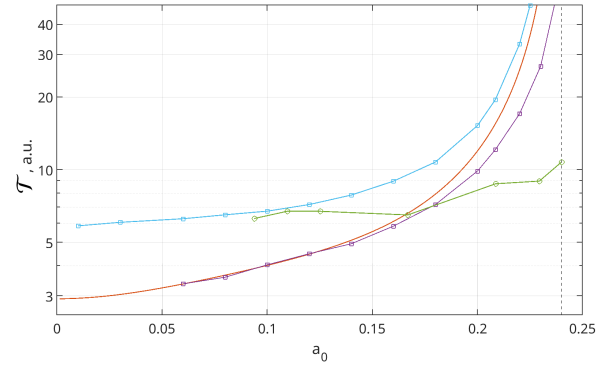


FIG. 9. **Period of the slow Coulomb induced oscillations during the interaction.** The period vs the field parameter  $a_0$ : (blue solid line, squares) the period extracted from the exact solution of Eq. (5) using the quantum average of the Coulomb potential [Eq. (6)], (magenta solid line, squares) the period extracted from the exact solution of Eq. (5) with the atomic potential of Eq. (8); (red solid line) the period extracted from the solution of the approximate Eq. (12)). Green line with circles – a period of oscillations of the quantum ionization probability. Dashed black line – the threshold  $a_0^{(th)}$ .

with the frequency

$$\Omega = \frac{\sqrt{Z}}{(a_s^2 + a_0^2)^{3/4}}. \quad (15)$$

The period of the slow oscillation  $\mathcal{T} = 2\pi/\Omega$  via the solution of simple approximate Eq. (12) (magenta line), and the exact numerical solution of Eq. (5) with the approximation Eq. (8) (red line) are shown in Fig. 9. Both results coincide quantitatively for the case  $a_0 < 0.13$ , and exhibit the same trend for the general case  $a_0 \rightarrow 0.25$ , which confirms the accuracy of the approximation in Eq. (12).

The oscillatory dynamical picture in the KH potential is valid when the drift distance during one slow oscillation  $\sim v_{zd}/\Omega$  does not exceed the Coulomb induced oscillation amplitude  $z_C$ :

$$v_{zd}/\Omega \lesssim z_C. \quad (16)$$

We estimate  $z_C$  from the energy conservation at Coulomb oscillation in the KH potential:

$$\frac{v_{zd}^2}{2} = \frac{Z}{\sqrt{a_s^2 + a_0^2 + z_C^2}}. \quad (17)$$

We may approximate in this regime  $\Omega \approx Z/a_0^{3/2}$ , and  $z_C \approx 2Z/v_{zd}^2$ , and the condition for the given dynamical picture is

$$a_0 \lesssim \left( \frac{16 \cdot 2^{2/3} Z \omega}{c^3} \right)^{1/5} \approx 0.2, \quad (18)$$

for  $\omega = 14$ ,  $Z = 2$ .

The periodicity of the ionization yield disappears at larger  $a_0$  [see the case of  $a_0 = 0.29$  in Figs. 1 and 5] when the drift

dominates the Coulomb force. We may estimate this threshold assuming the kinetic energy of the electron at switching-on the field  $v_{zd}^2/2$  exceeds the Coulomb attraction estimated by  $I_p = Z^2/2$ , which results in the condition

$$a_0 \gtrsim a_0^{(\text{th})} = \sqrt{\frac{4Z}{c}}, \quad (19)$$

for our case  $a_0^{(\text{th})} \approx 0.24$ .

In turn, the oscillation period of the ionization yield is extracted directly from the quantum calculations [Fig. 1] and is presented in Fig. 9 (green line). There is a qualitative accordance between the oscillation periods of the ionization yield and that of the  $\langle z \rangle$  expectation value via the classical estimate of the blue line for  $a_0 \lesssim 0.13$ , and of the magenta line within the interval  $0.15 \lesssim a_0 \lesssim 0.2$ . At larger  $a_0 \gtrsim 0.2$ , the period of the ionization yield does not significantly grow as  $a_0$  increases. It remains on the level, corresponding to the period of  $\langle z \rangle$  oscillations via the classical estimate for  $a_0 \lesssim 0.2$ . This stems from the fact, that during the interaction the electron is not represented as a single wave packet. In fact, one part of the electron wave packet always remains localized near the center of the Coulomb potential and experiences slow oscillations described by the analysis of the Ehrenfest equation. This part of the electron wave packet is responsible for the ionization yield oscillation. The other part of the wave packet drifts in the positive  $z$  direction,  $z_d = v_{zd}T$ , and is responsible for the gradual increase of the ionization yield with the duration of the pulse  $T$  [Fig.5]. After the end of the pulse, the shifted part of the electron is attracted back to the Coulomb center and diffracted by the atomic core, producing the spectrum in Fig. 7. The larger  $a_0$ , the more pronounced is the contribution from the drifted part of the electron, which results in the decrease of the oscillation magnitude, making the yield oscillation hardly visible as  $a_0 \rightarrow 0.29$  [Fig.5].

For the  $a_0$  values in the interval  $(0.2, 0.24)$  the oscillation period from the quantum calculations saturates, while the solution of the classical Eq. (12) shows an oscillation with an increasing period. The latter is possibly connected with the fact that the classical trajectories near the separatrix of the ionization threshold with a large oscillation period are actually ionized in the quantum treatment.

## V. PHOTON MOMENTUM SHARING BETWEEN THE PHOTOELECTRON AND ION

Here, we address the question of the partition of the momentum of absorbed photons between the ionized electron and the emerged ion in the case of the nondipole stabilization regime.

We begin with the energy and momentum conservation, which are fulfilled during the ionization process:

$$n\omega - I_p = \varepsilon_e + \varepsilon_i \quad (20)$$

$$\frac{n\omega}{c} = p_{ze} + p_{zi}, \quad (21)$$

where  $\varepsilon_e$  and  $\varepsilon_i$ ,  $p_{ze}$  and  $p_{zi}$  are the photoelectron and ion kinetic energies and momenta, respectively. The kinetic energy

of the ion can be neglected because of its large mass with respect to the electron, and the photoelectron energy determines the total number of absorbed photons. Then, the ion final momentum is

$$p_{zi} = (\varepsilon_e + I_p)/c - p_{ze}. \quad (22)$$

The photoelectron average momentum  $\langle p_{ze} \rangle$  and average energy  $\langle \varepsilon_e \rangle$  can be extracted directly from our simulation results, with  $I_p = Z^2/2$ , which are shown in Fig. 10 in the case of a short Gaussian pulse and different field intensities. A particular appearance of Fig. 10 depends on the length of the pulse  $N$  and its frequency  $\omega$ , although qualitatively the picture remains similar. We distinguish the momentum sharing for the near ZEP, from that of the ATI multiphoton peaks (mostly a single photon ionization peak is observed), because the physical origin of their momentum partition is different.

For the ZEP, the total momentum of the absorbed photons is approximately vanishing as expected, because it is produced with multiphoton absorption and emission of an equal number of photons. The average photoelectron momentum at large  $a_0$  is negative, which is known to emerge due to the CMT during the interaction and producing the angular peak in the laser counterpropagation direction [30]. For the ZEP CMT competes with the laser induced drift, because of which the sign of  $\langle p_{ze} \rangle$  changes at low  $a_0$ . It turns out, that for  $a_0 < 0.05$  the CMT is not strong enough to reverse  $p_{ze}$ . However, as  $a_0$  grows,  $p_{ze}$  becomes negative, increasing by module at least up to  $a_0 \approx 0.25$ .

For the ATI peaks, the total momentum of the absorbed photons is approximately  $\omega/c \approx 0.1$  as expected. The average photoelectron momentum is positive and decreasing with larger  $a_0$ ,  $\langle p_{ze} \rangle > \omega/c$ , which means that the ion momentum is negative (opposite to the photon momentum) and also decreasing with larger  $a_0$ .

We calculated also the  $\langle p_{ze} \rangle$  via the total PMD. It is known that for the low  $a_0$ , the ionization is dominated by the ATI process [19], and consequently,  $\langle p_{ze} \rangle$  via the total PMD coincides with that of the ATI. However, for  $a_0 > 0.1$  the Coulomb scattering takes over, the peak dominates, which results in a change of sign for  $p_{ze}$ . At some point  $a_0 \approx 0.1$ , ATI contribution and the ZEP contribution become equal, which results in a nearly zero photo-electron momentum along the laser propagation direction.

Finally, in order to prove that  $p_{ze} < 0$  for the ZEP is caused by CMT, we carried out a simple classical simulation. We create a classical ensemble of electrons mimicking the final electron wave packet. Both final coordinates  $\{x_f, z_f\}$  and  $\{p_{x_f}, p_{z_f}\}$  are sampled from the ZEP wave function density  $\psi(x, z, t_f)$ .  $\{p_{x_f}, p_{z_f}\} = -i\nabla\psi(x_f)/\psi(x_f)$ . Each trajectory is propagated backward in time classically until its energy  $\varepsilon(t) = [p(t) - p_L(t)]^2/(2m) + V < 0$ , where  $p_L(t)$  is a momentum of the same electron backward propagated only with the laser field. That point  $t_i$  is considered a moment of ionization. The CMT is calculated as  $p_C = - \int_{t_i}^{t_f} \nabla V(x(t'), z(t')) dt'$ . The CMT average over the ensemble is shown in Fig. 10. The CMT with the opposite sign represent the momentum transferred to the ion. As the total photon momentum for ZRP is vanishing, one expects the CMT to coincide with  $p_{ze}$ . While our simple

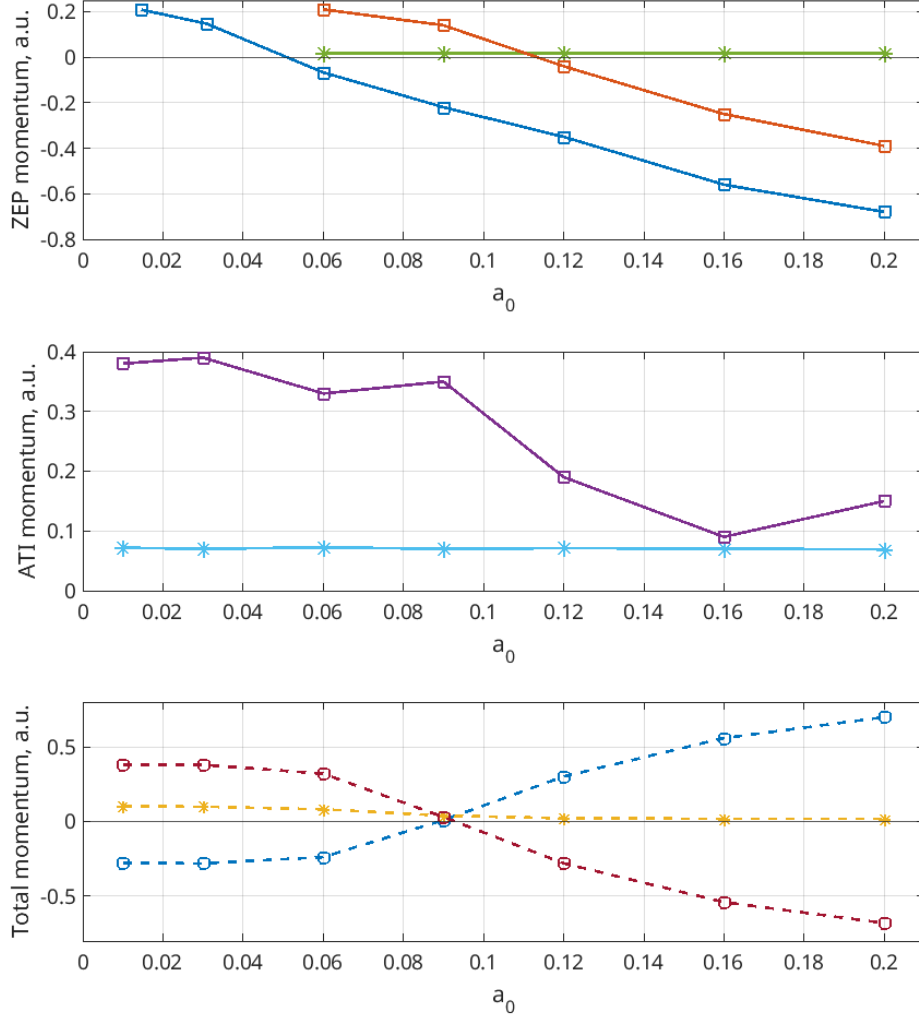


**FIG. 10. Momentum sharing between the photoelectron and ion vs the field parameter  $a_0$ .** For the ZEP: the average photoelectron momentum  $\langle p_{ze} \rangle$  – (blue solid line, squares), the total momentum of absorbed photons  $\langle n\omega/c \rangle = \langle \varepsilon_e + I_p \rangle/c$  – (green solid, stars), the CMT  $p_C$ , calculated via the pseudo-classical simulation (red solid line, squares). For ATI peaks (mostly the first peak):  $\langle p_{ze} \rangle$  – (magenta solid, squares);  $\langle n\omega \rangle/c$  – (light blue solid, stars). For the total PMD:  $\langle p_{ze} \rangle$  – (dashed brown line,  $\langle n\omega \rangle/c$  – (dashed yellow line, circles),  $\langle p_{zi} \rangle$  – (dashed blue line, squares).

estimate does not give coincidence, nevertheless it reproduces the trend of an actual  $p_{ze}$ , deviating only by a constant factor.

## VI. CONCLUSION

We have developed a method for the numerical solution of the Foldy-Wouthuysen transformed TDDE for the aim of treating the strong field ionization in the relativistic regimes. Our method is based on the coordinates scaling ansatz that absorbs as well the kinetic propagation phase of the wave function. The method is tested and analyzed in Ref. [53].

Using this method, we solve numerically 2D problem of the strong field ionization of a hydrogen-like helium atom in a high-frequency strong laser field. We have found a previously unobserved effect that the ionization yield in the stabilization regime oscillates with the laser pulse duration. While this effect exists in the dipole regime as well as in the nondipole one the underlying physical mechanism and the features of the yield oscillation are different.

In the dipole case, the yield oscillation has been explained by means of the dynamic interference phenomenon, combined with the electron periodic dynamics in the polarization direction in the KH potential.

In the nondipole case the ionization yield oscillation is a result of a more complex dynamics. The key point is the periodic slow oscillation along the laser propagation direction, which arises due to the competition between the laser induced drift and the Coulomb attraction. This slow oscillation brings about the varying average energy after the interaction and varying CMT, which finally results in the periodic variation of the ionization yield depending on the interaction time. We have estimated the scaling of the oscillation period and the threshold intensity when the drift dominates the ionization.

While in the nondipole regime, still the dynamic interference existed, however with the diminished role, the significant part of ionization emerges due to the asymmetric Coulomb momentum transfer to the electron wave packet during the continuum dynamics dominated by the nondipole drift. At first sight it seems the larger the nondipole drift, the larger is the asymmetry, and the larger should be the CMT. However, this picture overlooks the long term role of the Coulomb field for the electron dynamics in the continuum. Owing to the Coulomb field the electron wave packet features slow oscillations along with the nondipole drift. During turning points of this Coulomb orbiting the electron wave packet slows down acquiring a large CMT, which results in increasing the anomalous lobe in PMD and in the total ionization yield. This happens periodically when the duration of the laser pulse matches the multiples of the Coulomb orbiting period.

We have investigated also the absorbed photon momentum partition between the photoelectron and ion during the ionization in the nondipole stabilization regime. There are two characteristic features to underline. Firstly, the momentum partition is very different for the ZEP and ATI peaks. Secondly, the large Coulomb effect results in the ZEP photoelectron final average momentum being opposite to the laser propagation direction at large  $a_0$ , which however is reverted when  $a_0 \ll 1$ .

For the observation of the considered effect in the ionization in the stabilization regime, the strong x-ray field of about 400 eV photons is required with intensities reaching  $10^{21}$  W/cm<sup>2</sup>. For comparison, the present parameters of LCLS XFEL includes such photon energies, but with intensities of about  $10^{16}$  W/cm<sup>2</sup>, at the photon beam size of 16  $\mu\text{m}$  [56]. Therefore, to reach the required intensity one should face the challenge of x-ray focusing.

## Appendix A: Calculation methods

We consider a hydrogen-like ion in a strong laser field, describing the electron dynamics with the Dirac equation:

$$\begin{aligned} i\partial_t\psi &= H_D\psi & (A1) \\ H_D &= \beta c^2 + O + V, \\ O &= c\alpha\left(\mathbf{p} - \frac{e}{c}\mathbf{A}(\mathbf{r}, t)\right) \\ \mathbf{A}(\mathbf{r}, t) &= A(t - z/c)\mathbf{e}_x, \end{aligned}$$

where  $\alpha, \beta$  are the Dirac matrices,  $\mathbf{A}(\mathbf{r}, t)$  is the vector potential of the laser field,  $V(\mathbf{r}) = -Z/r$  is the atomic potential, with the charge  $Z$ , and  $e$  is the electron charge. We account for the nondipole effects using the laser vector potential as a propagating wave. To employ the coordinate scaling method [53], we apply the FW transformation to the Dirac Hamiltonian in Silenko's (quasiclassical) form [50] as an  $\hbar$  expansion:

$$\psi_{FW} = U_{FW}\psi = e^{iS_{FW}}\psi, \quad (A2)$$

arriving at the FW Hamiltonian [53]:

$$H_{FW} = \beta\varepsilon + V - \frac{1}{8} \left\{ \frac{1}{\varepsilon(\varepsilon + c^2)}, [O, [O, \mathcal{F}]] \right\} + O(\lambda^2) \quad (A3)$$

where  $\lambda$  is the Compton wavelength, and

$$\mathcal{F} = V - i\hbar\partial_t, \quad \varepsilon = c^2 \sqrt{1 + \frac{O^2}{c^4}}.$$

Introducing the magnetic field  $\mathbf{B} = \nabla \times \mathbf{A} = \partial_z A(t, z)\hat{\mathbf{e}}_y$ , the operator  $\varepsilon$  reads

$$\varepsilon = c^2 \sqrt{1 + \frac{(p_x - \frac{\varepsilon}{c}A(t, z))^2}{c^2} + \frac{p_z^2}{c^2} - \frac{e\hbar}{c^3}\Sigma_y \cdot B_y} \quad (A4)$$

where  $\Sigma$  is the spin operator. Taking into account  $\partial_z A(t, z) \sim \omega A(t, z)/c$ , and the smallness of the parameter  $a_0\lambda/\lambda$  for the applied parameters, with the laser wavelength  $\lambda$ , we obtain the expansion:

$$\begin{aligned} \varepsilon &= c^2\varepsilon_0(\mathbf{p}, t) - \frac{\lambda}{2\varepsilon_0(\mathbf{p}, t)}\Sigma_y \cdot B_y + O\left((a_0\lambda/\lambda)^2\right), \quad (A5) \\ \varepsilon_0(\mathbf{p}, t) &= \sqrt{1 + \frac{(p_x - \frac{\varepsilon}{c}A(t, z))^2}{c^2} + \frac{p_z^2}{c^2}}. \end{aligned}$$

As a result, there are no more matrices inside the square-root operator  $\varepsilon_0$ , which simplifies the calculations. However, the variables from different coordinate spaces, namely momenta  $p_x$  and  $p_z$  are still mixed with the regular coordinate  $z$ . In order to implement the square-root operator, we expand it into a Taylor series:

$$\begin{aligned} \varepsilon_0(\mathbf{p}, z, t) &= \sqrt{1 + X(\mathbf{p}, z, t)} \\ &= 1 + \frac{1}{2}X(\mathbf{p}, z, t) - \frac{1}{8}X(\mathbf{p}, z, t)X(\mathbf{p}, z, t) + \dots \quad (A6) \end{aligned}$$

Note, that the term  $X^2(\mathbf{p}, t)$  produces terms, proportional to  $\partial_z A(t, z)$  and  $\partial_{zz}^2 A(t, z)$  and so on. Thus, we single out the terms by the different orders of  $\partial_z^n A(t, z)$  and then roll back the expanded expressions inverting Eq. (A6)):

$$\varepsilon_0 = \sqrt{1 + \frac{(-i\partial_x - \frac{e}{c}A(t, \tilde{z}))^2}{c^2} - \frac{\partial_{zz}^2}{c^2}} - \frac{i}{2} \frac{1}{c^2} \frac{e}{c} \frac{\partial A(t, z)}{\partial z} \left[ \frac{(-i\partial_x - \frac{e}{c}A(t, \tilde{z}))(-i\hbar\partial_z)}{c} \right] \left[ 1 + \frac{(-i\partial_x - \frac{e}{c}A(t, \tilde{z}))^2}{c^2} - \frac{\partial_{zz}^2}{c^2} \right]^{-3/2} + O((a_0\lambda/\lambda)^2), \quad (\text{A7})$$

where the designation  $z = \tilde{z}$  means that derivative operators do not act on  $A(t, z)$ . In Eq. (A7) we omit terms, proportional to  $(\partial_z A(t, z))^2$  and  $\partial_{zz}^2 A(t, z)$  as of a high-order smallness. For the implementation of the first term in Eq. (A7), we again apply the Taylor expansion method and obtain an expression similar to the 1D case of Ref. [53]:

$$\begin{aligned} & \sqrt{1 + \frac{(-i\partial_x - \frac{e}{c}A(t, \tilde{z}))^2}{c^2} - \frac{\partial_{zz}^2}{c^2}} \phi(x, z) e^{i\varphi(x, z)} \\ &= \phi T_0(x, z, t) - i\lambda \left[ \phi'_x T_{1,x}(x, z, t) + \phi'_z T_{1,z}(x, z, t) \right] - \frac{\lambda^2}{2} \left[ \phi''_{xx} T_{2,xx}(x, z, t) + 2\phi''_{xz} T_{2,xz}(x, z, t) + \phi''_{zz} T_{2,zz}(x, z, t) \right] + O(\lambda^3/\ell^3), \end{aligned} \quad (\text{A8})$$

where we assume that  $\phi' \sim 1/\ell$  and  $\lambda/\ell \ll 1$ , i.e. function  $\phi$  does not contain large relativistic oscillations. The second term can be written in the same manner

$$\left[ \frac{(-i\hbar\partial_x - \frac{e}{c}A(t, \tilde{z}))(-i\hbar\partial_z)}{mc} \right] \left[ 1 + \frac{(-i\hbar\partial_x - \frac{e}{c}A(t, \tilde{z}))^2}{m^2 c^2} - \frac{\hbar^2 \partial_{zz}^2}{m^2 c^2} \right]^{-3/2} = \phi W_0(x, z, t) - i\lambda \left[ \phi'_x W_{1,x}(x, z, t) + \phi'_z W_{1,z}(x, z, t) \right] + O(\lambda^2/\ell^2) \quad (\text{A9})$$

where we omit some  $\lambda^2$  terms which have an additional smallness via  $\omega/c^2$ .

Recalling Eq. (A3) and using Eqs. (A4) and (A7), the FW Hamiltonian reads:

$$H_{FW} = \beta c^2 \varepsilon_0 - \frac{e\lambda}{2\varepsilon_0} \beta \Sigma_y \cdot B_y + V + \frac{e\lambda}{8c^3} \left\{ \frac{1}{\varepsilon_0(\varepsilon_0 + 1)}, [\Sigma \cdot (\boldsymbol{\pi} \times \tilde{\mathbf{E}} - \tilde{\mathbf{E}} \times \boldsymbol{\pi}) - \Delta V] \right\} + O(\lambda^2/\ell^2) \quad (\text{A10})$$

where  $\boldsymbol{\pi} = \mathbf{p} - \frac{e}{c}\mathbf{A}$ , and  $\tilde{\mathbf{E}} = \nabla V - \frac{1}{c}\dot{\mathbf{A}}$ . With the Hamiltonian Eq. (A10) and factorization  $\psi = \phi e^{i\varphi}$ , we arrive to the FW governing equation

$$\begin{aligned} i\partial_t \phi &= c^2 \left[ T_0(\xi R, t) - i\lambda \frac{T_1}{R} \cdot \partial_\xi - \frac{\lambda^2}{2} \frac{T_2}{R^2} \partial_{\xi\xi}^2 + O\left(\frac{\lambda^3}{\lambda_e^3}\right) \right] \phi + \frac{i}{2} \frac{\hbar e}{mc} \frac{\partial A(t, z)}{\partial z} \left( 1 + i\beta \Sigma_y \right) \left[ W_0(x, z, t) - i\lambda W_1 \cdot \partial_\xi + O\left(\frac{\lambda^2}{\lambda_e^2}\right) \right] \phi + \\ &+ \frac{\lambda e}{8c^3} \left\{ \frac{1}{\varepsilon_0^2(x, z, t) + \varepsilon_0(x, z, t)}, [\Sigma \cdot (\boldsymbol{\pi} \times \tilde{\mathbf{E}} - \tilde{\mathbf{E}} \times \boldsymbol{\pi}) - \Delta V] \right\} \phi + V(\xi R) \phi + \phi \left[ \dot{\phi} - \frac{\dot{R}}{R} \xi \cdot \partial_\xi \varphi \right] + i \frac{\dot{R}}{R} \xi \cdot \partial_\xi \phi + O(\lambda^2) \end{aligned} \quad (\text{A11})$$

where  $\phi(x, z, t)$  is a smooth envelope function,  $\phi' \sim 1/\ell$ ,  $T_i$  and  $W_i$  are smooth functions given in Appendix B in [53].

Further, we introduce the smooth phase in momentum space  $\varphi(t, x, z)$  ( $\varphi \gg \varphi'(t, x, z)\lambda$ ), using the following educated guess:

$$\hat{\varphi}(p_x, p_z, \tilde{z}, t) = - \int_0^t \sqrt{1 + \frac{(p_x - \frac{e}{c}A(t', \tilde{z}))^2}{m^2 c^2} + \frac{p_z^2}{m^2 c^2}} dt'. \quad (\text{A12})$$

Since  $\omega \ll c^2$  and  $\hat{\varphi}$  has to be smooth, it is enough to calculate Eq. (A12) for a few reference values  $\tilde{z}$  and then interpolate to obtain  $\hat{\varphi}(p_x, p_z, z, t)$  for any  $z$ . Interpolation can be done via, for example, splines, or with Chebyshev polynomials, because we are free to choose reference nodes  $\tilde{z}$ .

As a result, the procedure for the phase  $\varphi$  calculation at each time step  $\Delta t$  is the following:

1. Calculate

$$\hat{\varphi}(p_x, p_z, \tilde{z}, t) = \int_0^t \sqrt{1 + \frac{(p_x - \frac{e}{c}A(t', \tilde{z}))^2}{m^2 c^2} + \frac{p_z^2}{m^2 c^2}} dt' \text{ for every reference value } \tilde{z} \in [-L_z, L_z].$$

2. Interpolate  $\hat{\varphi}(p_x, p_z, \tilde{z}, t)$  to get  $\hat{\varphi}(p_x, p_z, z, t)$ .
3. Calculate critical points  $x_0(p_x, p_z) = -\frac{\partial \hat{\varphi}}{\partial p_x}$  and  $z_0(p_x, p_z) = -\frac{\partial \hat{\varphi}}{\partial p_z}$ .
4. Calculate the phase as  $\varphi(x)|_{x=x_0(p)} = \hat{\varphi}(p)p x_0(p)$ .
5. Rescale  $x' = \beta(t)x$  and  $z' = \beta(t)z$ . Since the set of points  $\{x_0, z_0\}$  is non uniform and does not make up a grid but rather a mesh, it complicates an interpolation  $\varphi(x, z) \rightarrow \varphi(x', z')$ . One can use different technics for the solving of optimization problem in order to interpolate from the 2D non uniform mesh to the other non uniform mesh.

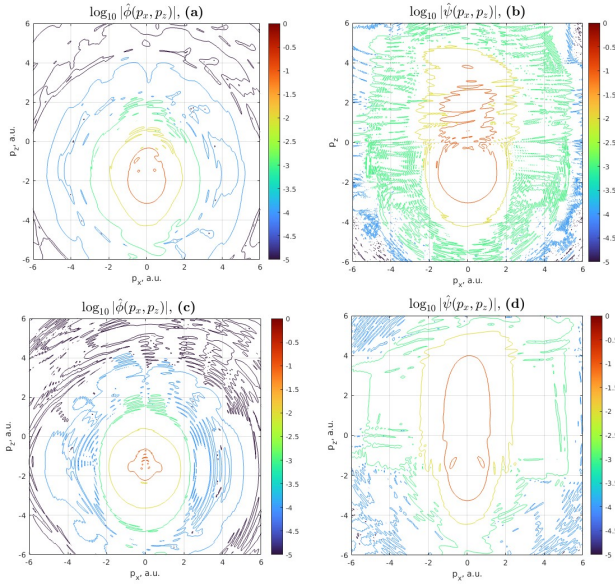


FIG. 11. The comparison of the envelope function  $|\hat{\phi}(\mathbf{p})|$  and the original wavefunction  $|\hat{\psi}(\mathbf{p})|$ . Parameters of the field:  $\omega = 14$  a.u.,  $E = 400$  a.u.,  $a_0 = 0.21$ . (a)  $\hat{\phi}(\mathbf{p})$  after 8 cycles, (b)  $\hat{\psi}(\mathbf{p})$  after 8 cycles, (c)  $\hat{\phi}(\mathbf{p})$  after 30 cycles, (d)  $\hat{\psi}(\mathbf{p})$  after 30 cycles

This algorithm provides us with a decent choice for the smooth phase  $\varphi$ . In Fig. 11 the module of the smooth envelope function  $\hat{\phi}(\mathbf{p})$  and the wave function  $\hat{\psi}(\mathbf{p})$  are presented. One sees that  $\hat{\phi}(\mathbf{p})$  is more narrow than  $\hat{\psi}(\mathbf{p})$ , and located closer to the origin, which means that in the coordinate space function  $\phi(\mathbf{x})$  is much more smooth than the wavefunction  $\psi(\mathbf{x})$ .

We have carried out relativistic simulations via Eq. (A11) and compare those with the results of the nondipole TDSE with the Hamiltonian:

$$H_{\text{nd}} = \frac{1}{2} \left[ p_x - \frac{e}{c} A(t, z) \right]^2 + \frac{1}{2} p_z^2 + V(r). \quad (\text{A13})$$

The linearly polarized laser pulse is of a trapezoidal form, with the vector potential  $A_x(\eta) = A_0 \sin(\omega\eta)$  in the flat part of the pulse, and with the rising and falling edges described as  $A_x(\eta) = A_0 e^{-2\ln(2)(\eta/\tau)} \sin(\omega\eta)$ , where  $\eta = t - z/c$  for the nondipole and  $\eta = t$  for the dipole cases.

---

[1] W. Becker, F. Grasbon, R. Kopold, D. B. Milošević, G. G. Paulus, and H. Walther, Above-threshold ionization: from classical features to quantum effects, *Adv. Atom. Mol. Opt. Phys.* **48**, 35 (2002).

[2] P. Agostini and L. F. DiMauro, The physics of attosecond light pulses, *Rep. Prog. Phys.* **67**, 813 (2004).

[3] P. B. Corkum and F. Krausz, Attosecond science, *Nature Phys.* **3**, 381 (2007).

[4] F. Krausz and M. Ivanov, Attosecond physics, *Rev. Mod. Phys.* **81**, 163 (2009).

[5] F. Krausz, Nobel lecture: Sub-atomic motions, *Rev. Mod. Phys.* **96**, 030502 (2024).

[6] A. L'Huillier, Nobel lecture: The route to attosecond pulses, *Rev. Mod. Phys.* **96**, 030503 (2024).

[7] P. Agostini, Nobel lecture: Genesis and applications of attosecond pulse trains, *Rev. Mod. Phys.* **96**, 030501 (2024).

[8] M. Altarelli, The european x-ray free-electron laser: toward an ultra-bright, high repetition-rate x-ray source, *High Power Laser Science and Engineering* **3**, e18 (2015).

[9] C. Bostedt, S. Boutet, D. M. Fritz, Z. Huang, H. J. Lee, H. T. Lemke, A. Robert, W. F. Schlotter, J. J. Turner, and G. J. Williams, Linac coherent light source: The first five years, *Rev. Mod. Phys.* **88**, 015007 (2016).

[10] M. Yabashi, H. Tanaka, T. Tanaka, H. Tomizawa, T. Togashi, M. Nagasano, T. Ishikawa, J. R. Harries, Y. Hikosaka, A. Hishikawa, K. Nagaya, N. Saito, E. Shigemasa, K. Yamouchi, and K. Ueda, Compact XFEL and AMO sciences: SACLA and SCSS, *J. Phys. B* **46**, 164001 (2013).

[11] J. Fan, Y. Tong, Y. Nie, and *et al.*, First commissioning results of the coherent scattering and imaging endstation at the shanghai soft x-ray free-electron laser facility, *Nucl. Sci. Techn.* **33**, 114 (2022).

[12] S. Walker and A. Landsman, Above-threshold ionization with x-ray free-electron lasers, *Commun. Phys.* **7**, 353 (2024).

[13] V. C. Reed and K. Burnett, Ionization of atoms in intense laser pulses using the kramers-henneberger transformation, *Phys. Rev. A* **42**, 3152 (1990).

[14] A. Patel, N. J. Kylstra, and P. L. Knight, Effect of laser pulse shapes on the stabilization of a model atom, **32**, 5759 (1999).

[15] M. Gavrila, Atomic stabilization in superintense laser fields, *Journal of Physics B: Atomic, Molecular and Optical Physics* **35**, R147 (2002).

[16] H. A. Kramers, *Collected Scientific Papers* (North-Holland, Amsterdam, 1956) p. 272.

[17] W. C. Henneberger, Perturbation method for atoms in intense light beams, *Phys. Rev. Lett.* **21**, 838 (1968).

[18] S. Azizi, U. Saalmann, and J. M. Rost, Zero-energy photoelectric effect, *Phys. Rev. Lett.* **134**, 103201 (2025).

[19] D. A. Telnov and S.-I. Chu, Relativistic ionization probabilities and photoelectron distributions of hydrogenlike ions in super-strong electromagnetic fields, *Phys. Rev. A* **104**, 023111 (2021).

[20] M. Protopapas, C. H. Keitel, and P. L. Knight, Relativistic mass shift effects in adiabatic intense laser field stabilization of atoms, *Journal of Physics B: Atomic, Molecular and Optical Physics* **29**, L591 (1996).

[21] L. N. Gaier and C. H. Keitel, Relativistic classical monte carlo simulations of stabilization of hydrogenlike ions in intense laser pulses, *Phys. Rev. A* **65**, 023406 (2002).

[22] A. Staudt and C. H. Keitel, Stabilization of helium in intense high-frequency laser pulses beyond the dipole approximation, *Journal of Physics B: Atomic, Molecular and Optical Physics* **36**, L203 (2003).

[23] M. Protopapas, C. H. Keitel, and P. L. Knight, Atomic physics with super-high intensity lasers, *Reports on Progress in Physics*

60, 389 (1997).

[24] C. H. Keitel and P. L. Knight, Monte carlo classical simulations of ionization and harmonic generation in the relativistic domain, *Phys. Rev. A* **51**, 1420 (1995).

[25] A. Di Piazza, C. Müller, K. Z. Hatsagortsyan, and C. H. Keitel, Extremely high-intensity laser interactions with fundamental quantum systems, *Rev. Mod. Phys.* **84**, 1177 (2012).

[26] <https://lcls.slac.stanford.edu/machine/parameters> () .

[27] M. Dondera and H. Bachau, Exploring above-threshold ionization of hydrogen in an intense x-ray laser field through nonperturbative calculations, *Phys. Rev. A* **85**, 013423 (2012).

[28] M. Klaiber, K. Z. Hatsagortsyan, and C. H. Keitel, Above-threshold ionization beyond the dipole approximation, *Phys. Rev. A* **71**, 033408 (2005).

[29] M. Klaiber, K. Z. Hatsagortsyan, and C. H. Keitel, Relativistic ionization rescattering with tailored laser pulses, *Phys. Rev. A* **74**, 051803 (2006).

[30] M. Førre, J. P. Hansen, L. Kocbach, S. Selstø, and L. B. Madsen, Nondipole ionization dynamics of atoms in superintense high-frequency attosecond pulses, *Phys. Rev. Lett.* **97**, 043601 (2006).

[31] Z. Zhou and S.-I. Chu, Multiphoton above-threshold ionization in superintense free-electron x-ray laser fields: Beyond the dipole approximation, *Phys. Rev. A* **87**, 023407 (2013).

[32] A. Ludwig, J. Maurer, B. W. Mayer, C. R. Phillips, L. Gallmann, and U. Keller, Breakdown of the dipole approximation in strong-field ionization, *Phys. Rev. Lett.* **113**, 243001 (2014).

[33] I. A. Ivanov, Spin-flip processes and nondipole effects in above-threshold ionization of hydrogen in ultrastrong laser fields, *Phys. Rev. A* **96**, 013419 (2017).

[34] A. Sommerfeld and G. Schur, Über den photoeffekt in der k-schale der atome, insbesondere über die voreilung der photoelektronen, *Annalen der Physik* **396**, 409 (1930), <https://onlinelibrary.wiley.com/doi/pdf/10.1002/andp.19303960402>.

[35] M. J. Seaton, Momentum transfer in photo-ionization processes, *Journal of Physics B: Atomic, Molecular and Optical Physics* **28**, 3185 (1995).

[36] C. T. L. Smeenk, L. Arissian, B. Zhou, A. Mysyrowicz, D. M. Villeneuve, A. Staudte, and P. B. Corkum, *Phys. Rev. Lett.* **106**, 193002 (2011).

[37] M. Klaiber, E. Yakaboylu, H. Bauke, K. Z. Hatsagortsyan, and C. H. Keitel, Under-the-barrier dynamics in laser-induced relativistic tunneling, *Phys. Rev. Lett.* **110**, 153004 (2013).

[38] S. Chelkowski, A. D. Bandrauk, and P. B. Corkum, Photon momentum sharing between an electron and an ion in photoionization: From one-photon (photoelectric effect) to multiphoton absorption, *Phys. Rev. Lett.* **113**, 263005 (2014).

[39] D. Cricchio, E. Fiordilino, and K. Z. Hatsagortsyan, Momentum partition between constituents of exotic atoms during laser-induced tunneling ionization, *Phys. Rev. A* **92**, 023408 (2015).

[40] S. Chelkowski, A. D. Bandrauk, and P. B. Corkum, Photon-momentum transfer in multiphoton ionization and in time-resolved holography with photoelectrons, *Physical Review A* **92**, 051401 (2015).

[41] A. Hartung, S. Eckart, S. Brennecke, J. Rist, D. Trabert, K. Fehre, M. Richter, H. Sann, S. Zeller, K. Henrichs, et al., Magnetic fields alter strong-field ionization, *Nat. Phys.* **15**, 1222 (2019).

[42] P.-L. He, M. Klaiber, K. Z. Hatsagortsyan, and C. H. Keitel, Nondipole coulomb sub-barrier ionization dynamics and photon momentum sharing, *Phys. Rev. A* **105**, L031102 (2022).

[43] X. Mao, H. Ni, K. Lin, P.-L. He, H. Liang, S. Eckart, F. He, K. Ueda, R. Dörner, and J. Wu, Photon momentum transfer and partitioning: from one to many, *Nature Communications* **16**, 5977 (2025).

[44] K. Toyota, O. I. Tolstikhin, T. Morishita, and S. Watanabe, Siegert-state expansion in the kramers-henneberger frame: Interference substructure of above-threshold ionization peaks in the stabilization regime, *Phys. Rev. A* **76**, 043418 (2007).

[45] K. Toyota, O. I. Tolstikhin, T. Morishita, and S. Watanabe, Interference substructure of above-threshold ionization peaks in the stabilization regime, *Phys. Rev. A* **78**, 033432 (2008).

[46] P. V. Demekhin and L. S. Cederbaum, Dynamic interference of photoelectrons produced by high-frequency laser pulses, *Phys. Rev. Lett.* **108**, 253001 (2012).

[47] W.-C. Jiang and J. Burgdörfer, Dynamic interference as signature of atomic stabilization, *Opt. Express* **26**, 19921 (2018).

[48] M.-X. Wang, H. Liang, X.-R. Xiao, S.-G. Chen, W.-C. Jiang, and L.-Y. Peng, Nondipole effects in atomic dynamic interference, *Phys. Rev. A* **98**, 023412 (2018).

[49] L. Geng, H. Liang, K. Krajewska, L.-Y. Peng, and Q. Gong, Laser-induced electron fresnel diffraction by xuv pulses at extreme intensity, *Phys. Rev. A* **104**, L021102 (2021).

[50] A. J. Silenko, Foldy-wouthuysen transformation and semiclassical limit for relativistic particles in strong external fields, *Phys. Rev. A* **77**, 012116 (2008).

[51] A. Y. Silenko, Comparative analysis of direct and “step-by-step” foldy-wouthuysen transformation methods, *Theoretical and Mathematical Physics* **176**, 987 (2013).

[52] A. J. Silenko, General method of the relativistic foldy-wouthuysen transformation and proof of validity of the foldy-wouthuysen hamiltonian, *Phys. Rev. A* **91**, 022103 (2015).

[53] A. V. Boitsov, K. Z. Hatsagortsyan, and C. H. Keitel, Scaling method for the numerical solution of the strong-field ionization problem in the relativistic regime, *Computer Physics Communications* **310**, 109511 (2025).

[54] A. Tasnim Aynul, L. C. Rodriguez, and C. F. d. M. Faria, Quantum beating and cyclic structures in the phase-space dynamics of the kramers-henneberger atom, *Phys. Rev. A* **111**, 043102 (2025).

[55] Y. I. Salamin and F. H. M. Faisal, Harmonic generation by superintense light scattering from relativistic electrons, *Phys. Rev. A* **54**, 4383 (1996).

[56] <https://lcls.slac.stanford.edu/sites/default/files/2024-07/LCLS-Parameters-Run-24.pdf> () .